# Energy Advances

## Accepted Manuscript

This article can be cited before page numbers have been issued, to do this please use: S. Hussain, M. Zimik, M. Devi, M. Kasif and R. Thangavel, *Energy Adv.*, 2025, DOI: 10.1039/D5YA00130G.




ROYAL SOCIETY OF CHEMISTRY

rsc.li/energy-advances

View Article Online
DOI: 10.1039/D5YA00130G



# 2D Layered $VSe_2$ with High Pseudocapacitive Zn-ion Storage as Cathode for High-Power Zinc-Ion Batteries

*Saddam Hussain[a], Mayanmi Zimik[a], Meghali Devi[a], Md Kasif[b], Ranjith Thangavel[a,b]**

[a] *School of Energy Science and Engineering, Indian Institute of Technology Guwahati, Guwahati 781039, India*

[b] *Department of Chemical Engineering, Indian Institute of Technology Tirupati, Tirupati 517619, India*

## Abstract

Aqueous zinc-ion batteries (ZIBs) are attractive storage solution for renewable energy storage systems (ESS) applications. Despite intrinsic safety, eco-friendliness, and low cost of aqueous ZIBs, their practical application is severely hindered by unavailability of high capacity and robust cathode materials. Vanadium-based cathodes with various structures, large layer spacing, and different oxidation states are considered suitable cathode candidates for ZIBs. In this work we studied 2D layered $VSe_2$ with high pseudocapacitive mediated Zn-ion storage as cathode for aqueous Zinc-Ion Batteries. The $VSe_2$ cathode reversibly hosted Zinc ion with a capacity of 205 mAh $g^{-1}$ at 0.2 A $g^{-1}$, maintaining a capacity of 135 mAh $g^{-1}$ at 8 A $g^{-1}$, and stability of 98% after 600 cycles at 1 A $g^{-1}$, favoured by 2D layered structure with defects and metallic conducting nature. Zn-ion storage mechanism and kinetics in the cathode is examined using ex-situ XRD, XPS, TEM, and GITT studies, and it is found that the favourable interlayer spacing with structural defects efficiently stored Zn-ion through high contribution from capacitive mediated storage. The favourable architecture enables fast Zn-ion diffusion, high capacity at high current rate along with good stability. The current work emphasizes on the potential of rational design of several transition metal dichalcogenides based cathode with strong pseudocapacitive storage for sustainable energy storage system like aqueous ZIB.

**Keywords**: $VSe_2$, Zinc-ion batteries, metal chalcogenides, 2D structure, pseudocapacitive

## 1. Introduction

As the world strives for carbon neutrality, the demand for advancements in electrochemical energy storage technologies has surged [1–4] . Lithium-ion batteries, the most commonly used storage device in portable electronic devices and electric vehicles, has cost limitations due to scarcity & uneven distribution of Li and Co reserves and potential hazards associated with use

* Corresponding author. Email: ranjith.t@iittp.ac.in; ranjith.t@iitg.ac.in

View Article Online
DOI: 10.1039/D5YA00130G



of volatile and combustible organic electrolytes [5,6]. The growing demand of energy storage devices for renewable energy storage devices in grid applications cannot be met by Li-ion batteries. In contrast, aqueous ion batteries are gaining much momentum due to computability with aqueous electrolyte, high ionic conductivity, environmental friendliness, and low cost, making them an ideal solution for large-scale energy storage applications to meet elevating global energy demands. Since multiple electrons are involved in the redox processes in multivalent metal ions like $Al^{3+}$, $Ca^{2+}$, $Mg^{2+}$ and $Zn^{2+}$, aqueous batteries can theoretically deliver high energy densities. Among multiple aqueous rechargeable batteries, zinc ion batteries (ZIBs) stand out with advantages like low cost, sustainability, elevated safety, high energy density. The utilization of Zn anode with a superior theoretical capacity of 820 mAh $g^{-1}$ offers high energy density along with excellent chemical stability, durability in aqueous electrolyte, making the system more attractive[7–11].

Currently, lack of suitable cathode material primarily limits advancements in ZIBs owing to. Zn's unique electrochemistry places significant restrictions on cathode materials, like exhibiting large capacity while being stable at high voltage. When Zn insertion produces adequate redox kinetics and high ionic/electronic transport in the cathode material & cathode/electrolyte interface, considerable gravimetric power density and rate performance can be observed [12–15]. Again, the structural integrity of the cathode material ensures cyclic stability in ZIBs.

The capacity, energy density, power density, rate performance, and stability of the ZIBS are governed by the cathode material. In the past decade, various Mn based compounds (α, β, γ-$MnO_2$, $ZnMnO_2$, $KMnO_2$, $MgMn_2O_4$ etc.), V based compounds (vanadium oxides, $Na_3V_2(PO_4)_3$ etc.), Prussian blue analogues, and organic compounds are studied for cathode material in ZIBs [16]. However, the complex structural transformations in manganese-oxide-based cathodes can trigger significant volume changes and a transition to an electrochemically inactive spinel phase, which leads to rapid capacity degradation. Although several polyanion compounds and Prussian blue cathodes exhibited reasonable working potential, their low specific capacity from large sized structure result in low gravimetric energy density. Vanadium oxide-based cathode showed high capacity with favourable 2D structure and fast diffusion. The multiple valance states ($V^x$, x=2+, 3+, 4+ 5+) in vanadium-based compounds have helped to storage large amount of Zn-ion into their structure, delivering high capacity [5,17,18]. Numerous V based cathode material including $V_xO_y$, vanadium phosphates and metal vanadate showed promising results for Zn-ion battery commercialization. However, the low voltage, and 2D

View Article Online
DOI: 10.1039/D5YA00130G



structure, the strong electrostatic interaction between the cathode material and divalent Zn ions results in low energy density, sluggish kinetics and poor cyclability.

Recently, layered transition-metal sulfides, a 2D compound held together by weak van der Waals forces, have gained significant attention for use in various energy storage devices, including Li-ion batteries, sodium-ion batteries, and supercapacitors. Due to their tunable interlayer spacing, abundant edge sites for Zn-ion storage, higher polarizability of sulfur anions compared to oxygen anions, and the presence of sulfur vacancies, transition metal sulfide cathodes have demonstrated high capacity at elevated voltages, along with excellent stability. Several transition metal cathodes based on $MS_2$, (M =Mo, W, V) were studied as cathode for ZIBs, and several strategies including morphology control, structural engineering, surface coating, and composite were employed to improve the electrochemical performance of $MS_2$ cathodes.

In recent days, exploring transition metal selenide-based materials is gaining much momentum. The selenide-based materials show superior metallic like electron conductivity, graphene-like 2D layered structure with through Van-der Waal stacking could allow rapid ion transport and storage. Se ions have a larger atomic radius and weaker electronegativity, making M-Se bond weaker compared to M-O and M-S counterparts, helping with lower polarization and increased reversibility during ion storage. Moreover, the low electronegativity of Se in comparison to O or S reduces the ion migration barrier, enhancing ion/electron transport. Transition metal selenides based on $VSe_2$, $WSe_2$, $TiSe_2$, $CuSe_2$, and $MnSe_2$, were recently explored as potential cathode for multivalent ion battery [19–22].

Among several explored transition metal selenides (TMS), $VSe_2$ is of high interest as they have naturally large interlayer spacing (0.61 nm) with higher electronic conductivity ($1.0 \times 10^3$ S $m^{-1}$) than $VS_2$ (9.907 S $m^{-1}$) due to the metallic nature of Se. The electron coupling force between the neighbouring $V^{4+}$–$V^{4+}$ atom outputs metallic feature which along with large interlayer spacing could synergistically provide the abundant channels and active sites to store Zn-ions. $VSe_2$ is emerging as favourable host material for zinc ions in ZIBs, that could deliver high capacity and fast Zn-ion storage [22–26]. However, $VSe_2$ often faces drawbacks like poor conductivity and low cycle stability when used for energy storage applications as they are always produced in bulk [27]. The electrochemical performance for TMSs can be optimized using methods like defect engineering, doping and carbon hybrids [27]. TMSs-nano carbon hybrid often provides synergetic advantages by enhancing electronic conductivity and providing

View Article Online
DOI: 10.1039/D5YA00130G



abundant internal pores, which improves the electron/ion diffusion kinetics. The multiwalled carbon nanotubes (MWCNT) can impart structural stability with improved conductivity and more efficient ion transfer channels. The unique $VSe_2$ – MWCNT nano hybrid could facilitates smooth electron transfer by providing pathways for fast electron/ion transfer, facilitating facile Zn-ion storage [28,29]. Furthermore, the Zn-ion storage mechanism in transition metal selenides is poorly understood which needs deeper investigation.

Herein, we propose a $VSe_2$-MWCNT composite as cathode material to host $Zn^{2+}$ ions in an aqueous Zn-ion battery. This work aims to incisively ameliorate the structural and electrochemical properties of $VSe_2$ nanosheets with incorporation of MWCNTs for reversible Zn-ion storage. Although $VSe_2$ based cathode materials were previously studied for Zn-ion batteries, we demonstrate a rationally designed $VSe_2$–MWCNT hybrid composite, and deeply investigated the Zn-ion storage mechanism. Hybrid architecture containing 2D layered $VSe_2$ over 1D multi-walled CNTs synergistic overcome the intrinsic restacking and conductivity limitations of pristine $VSe_2$. Furthermore, the selenium vacancy–rich sites in promoted reversible $Zn^{2+}$ intercalation, providing new insights into defect-assisted fast pseudocapacitive storage (92.62% at 0.5 mV $s^{-1}$) in layered selenides. The synergy of the two-dimensional $VSe_2$ nanosheets and MWCNTs results in superior capacity of 205 mAh $g^{-1}$ at 0.2 A $g^{-1}$.

In this work, we have studied few layered $VSe_2$ - MWCNT nano hybrid as cathode material to host $Zn^{2+}$ ions in an aqueous Zn-ion battery. The synergistic effect of the few layered $VSe_2$ nanosheets with MWCNT nano hybrid shows superior reversibility, showing a capacity of ~208, 205, 198, 185, 168, 134 mAh $g^{-1}$ at 0.2, 0.4,1, 2, 4, 8 A $g^{-1}$ respectively. The high-rate capability along with high stability is favoured by 2D layered structure with defects and metallic conducting nature, which surpasses many previously reported vanadium-based cathodes. Further deep investigation on Zn-ion storage mechanism using ex-situ XRD, XPS, TEM, and GITT revealed that the favorable 2D layered structure in transition metal selenides with large interlayer underwent pseudocapacitive type intercalation storage in Zn-ion battery.

## 2. Experimental section

### 2.1. Synthesis of $VSe_2$ and $VSe_2$-MWCNT

$VSe_2$ nanoflakes were synthesized by one step hydrothermal method. 1 mmol of vanadium pentoxide ($V_2O_5$) and 4 mmol of selenium dioxide ($SeO_2$) was thoroughly dispersed in DI water under constant stirring. This is followed by gradual addition of 19.5 mmol of oxalic acid ($C_2O_4H_2$) and the mixture was hydrothermally treated at 200 ºC for 24 h using a Teflon lined

View Article Online
DOI: 10.1039/D5YA00130G



stainless steel autoclave. The $VSe_2$ powders were collected by centrifugation and thoroughly washed with DI water and acetone and dried using vacuum oven at 60 ºC for 6 h. For the synthesis of $VSe_2$-MWCNT composite, an aqueous dispersion of 5 wt % MWCNT was added to the mixture while stirring and other procedure remains same. The MWCNT dispersion in DI water purchased from local vendor was used without any pretreatment. The MWCNTs was again dispersed in DI water through probe sonicator for 30 min.

### 2.2. Physical characterization

The crystal structure of the synthesized materials was studied with an X-ray diffractometer (Rigaku Smart Lab, X-ray source Cu Kα, λ=1.54 Å) at a scan rate of 5°/min. The surface morphology and microstructure of the materials were analysed with Field Emission Scanning Electron Microscope (Sigma 300) at 5 kV and Field Emission Transmission Electron Microscope (JEOL, JEM-2100F) with an operating voltage of 200 kV. SAED pattern of the synthesized materials were also obtained using JEOL, JEM-2100F instrument. The surface chemical environment was evaluated by X-ray photoelectron spectroscopy (XPS) with an ESCALAB Xi+ (Thermo Fisher Scientific, X-ray source: Al Kα). Laser Micro Raman System with wavelength 633 nm (Horiba Jobin Vyon, Model: LabRam HR) was used to preform Raman spectroscopy. High-Temperature Differential Scanning Calorimetry (DSC)/Thermo Gravimetric (TG) System (Netzsch Model: STA449F3A00) was used to perform Thermogravimetric analysis (TGA).

### 2.3. Electrochemical characterization

A homogeneous cathode slurry was prepared with $VSe_2$@MWCNT, carbon black and PVDF in an 8:1:1 weight ratio in NMP solvent and was cast over stainless steel (SS) foil using the doctor blade. The slurry-coated SS foil was further vacuum dried at 60ºC. Zn foil of diameter 12 mm was used as a counter electrode to investigate the electrochemical performance in a CR-2032-coin cell assembled under ambient conditions utilising 3M $Zn(CF_3SO_3)_2$ aqueous electrolyte. The mass loading of the cathode is ~2.5 mg $cm^{-2}$, and the diameter of the cathode is 12 mm. All electrochemical characterisations were carried out with an Origalys Workstation.

## 3. Results and discussion

### 3.1. Physical characterizations

The X-ray diffraction pattern of $VSe_2$ in **Figure 1a** shows a crystalline structure and confirms the pure phase details $VSe_2$ and $VSe_2$-MWCNT hybrids (JCPDS file No. 89-1641). The $VSe_2$

View Article Online
DOI: 10.1039/D5YA00130G



structure is attributed to hexagonal crystal structure with space group *P-3ml* and the calculated lattice parameters were a = b = 0.336 nm, c = 0.611 nm. The XRD patterns of $VSe_2$-MWCNT hybrids have an additional peak at 2θ = 26º due to (002) plane after incorporation of CNT hybrids. The Raman spectra of $VSe_2$ cathode in **Figure 1b** shows two peaks, centred around 145 $cm^{-1}$ ($E_2g$) and 205 $cm^{-1}$ ($A_1g$), corresponding to first order in-plane atomic vibrations inside Se – V layers and out-of-plane perpendicular vibration modes to Se layers. The $E_{2g}$ and $A_{1g}$ peaks in the $VSe_2$-MWCNT are shifted to the higher wave number due to the lattice distortion and selenium vacancies due to the presence of few-layered morphology and highly conductive MWCNT network. [24,30,31]. The presence of MWCNT in $VSe_2$ nanohybrid displayed the typical D and G bands of carbon at 1326 $cm^{-1}$ and G band at 1587 $cm^{-1}$ in the Raman spectra. The $I_D/I_G$ ratio of 1.63 in the $VSe_2$-MWCNT nanohybrid indicates a higher defect density in the hybrid. The presence of layered structure along with defects in the 2D layered $VSe_2$-MWCNT nanohybrid could provide lot of active sites for Zn-ion storage, enhanced Zn-ion diffusion, and a strong interface interface[32]. The hybrid architecture can control particle detachment by immobilizing the $VSe_2$ sites during volume changes with Zn-ion (de)intercalation and thus increase the stability, and rate capability of the hybrid.

The TGA analysis of the $VSe_2$ and $VSe_2$-MWCNT composite in **Figure S1** shows the change in weight as a function of temperature to monitor thermal stability as well as weight% of MWCNT in the composite. For both materials, after initial weight loss with evaporation of chemisorbed water around 100 ºC, and at ~200 ºC the weight of $VSe_2$@MWCNT slightly increases. The functional groups present in the porous MWCNTs may facilitate the oxidation of $VSe_2$. As MWCNTs - $VSe_2$ hybrid have high surface area, and at ~ 200 °C, oxygen can chemisorb onto defect sites or edges, leading to slight mass uptake[33]. A steep weight loss was observed between 375 ºC- 525 ºC. The $VSe_2$ material didn't show any weight loss after 525 ºC, however, the $VSe_2$-MWCNT composite material realised 8.8% weight loss which is attributed to decomposition of carbonaceous framework of the MWCNT. The field emission scanning electron microscopy (FE-SEM) images of pristine $VSe_2$ (Figure S2a-b) show nanoplate morphology with a thickness of ~5 nm, forming a hierarchical spherical flower-like morphology. However, the FE-SEM image $VSe_2$-MWCNT nanohybrids (Figure 1c-d) shows densely packed and non-agglomerated $VSe_2$ particles over CNTs sheets. The severe particle agglomeration was strongly inhibited by the presence of the CNT conductive network. The $VSe_2$-MWCNT nanohybrids displays evenly dispersed MWCNT interconnecting the $VSe_2$ flakes. This interlinked network of $VSe_2$ flakes in MWCNT hybrids favor rapid electron

View Article Online
DOI: 10.1039/D5YA00130G





transfer through the hybrid cathode material, enhancing material utilization at high current rate. This hierarchical flower-like surface morphology ensures enhanced participation of more redox active sites for Zn-ion (de)intercalation with increased surface area. **Figure 1e-f and Figure S2c** shows the FETEM image where 2D sheet like morphology of the $VSe_2$ is evident with diameter ~500 to 600 nm. The HR-TEM images of $VSe_2$-MWCNT nanohybrids (**Figure 1g**) clearly shows the lattice fringes, confirming its highly crystalline nature with d-spacing of 0.61 nm (**inset**: **Figure 1g**), corresponding to (002) plane of $VSe_2$. The elemental mapping of $VSe_2$-MWCNT (**Figure S2d**) using HAADF technique shows uniform distribution of V, Se and C elements as shown in figure 2d-g.

The surface chemical environment of the $VSe_2$-MWCNT composite material is analysed with XPS technique. The presence of V, Se and C elements are confirmed with XPS survey spectrum as shown in **Figure 2a**. In **Figure 2b**, the characteristic peaks for $V^{4+}$ $2p_{1/2}$ and $V^{4+}$ $2p_{3/2}$ are observed at 524 eV and 517.8 eV in the deconvoluted spectrum of V 2p. The $V^{4+}$ based vanadium materials tend to have metallic with favorable electron transport behaviour during cycling than $V^{5+}$ based vanadium phases which are insulating or semi-conducting. This facilitates reversible redox reactions during Zn-ion storage and better structural stability during repeated intercalation and deintercalation. Moreover, vanadium compounds with $V^{4+}$ to $V^{3+}$ redox shows open framework, helping to accommodate Zn-ions without structural degradation. However, vanadium compounds with $V^{5+}$ to $V^{4+}$ could suffer from structural distortion[34]. This can be correlated to the effects of phase transition during redox process which are crucial for capacity retention in sodium-ion and lithium-ion batteries[35,36]. Some $V^{3+}$ is also observed in the compound, indicating the presence of defects in $VSe_2$ cathode, and this could be attributed to Se vacancies or intrinsic electron distribution. Such are defects are beneficial for Zn-ion storage as the defects could lower the $Zn^{2+}$ insertion energy barrier and provide open up diffusion channels or interstitial sites for more Zn-ion storage [20]. The deconvoluted spectrum Se 3d spectrum in **Figure 2c** shows the characteristic peak for Se $3d_{3/2}$ and Se $3d_{5/2}$ at binding energies 55.2 eV and 56.3 eV in figure 3c [32,37]. The C1s can be deconvoluted (**Figure 2d**) to C-C bonds (285.1 eV), C-O bonds (285.1 eV) as well as C=O bonds (290.43 eV). The presence of C-O interactions in the composite material increases the electrode wettability towards the electrolyte with increased hydrophilicity for efficient charge storage with $VSe_2$-MWCNT composite material. Along with the peak for $sp^2$ hybridized C atoms, another satellite peak due to graphitic nature of the MWCNT is observed which confirms the structural intactness of MWCNT in the composite [30,31]. The MWCNT can offer structural stability of the composite

View Article Online
DOI: 10.1039/D5YA00130G



during charge/discharge as well as facilitate Zn ion intercalation in the $VSe_2$ layers. Again, the incorporation of highly conductive MWCNT in the composite adds porous conducting channels and surface defects to the layered $VSe_2$ architecture for reduced diffusion distance for Zn ion and allow enhanced influx of Zn ions in a brief period [24,38]. This design is promising to diminish interfacial resistance and increase the electrode-electrolyte interfacial area.

### 3.2. Electrochemical characterization

The electrochemical performance of the pristine $VSe_2$ and the $VSe_2$-MWCNT nanohybrid cathodes was systematically evaluated through cyclic voltammetry (CV) and galvanostatic charge–discharge (GCD) studies in the voltage window 0.2-1.6 V. **Figure 3a** compares the CV curves of pristine $VSe_2$ and $VSe_2$-MWCNT at 0.5 mV $s^{-1}$. The CV curves of $VSe_2$-MWCNT nanohybrid shows a sharper and more intense redox peaks with smaller polarization than pristine $VSe_2$, indicating faster $Zn^{2+}$ insertion/extraction kinetics along with enhanced electrochemical reversibility. The incorporation of MWCNTs network effectively improves electronic conductivity of $VSe_2$, enhancing the active material utilization for Zn-ion storage. The GCD curves in **Figure 3b** clearly demonstrate the superior electrochemical behaviour of $VSe_2$-MWCNT nanohybrid than pristine $VSe_2$. The $VSe_2$-MWCNT nanohybrid shows a discharge capacity of 214 mAh $g^{-1}$ at 0.4 A $g^{-1}$ while pristine $VSe_2$ showed only a capacity of ~140 mAh $g^{-1}$. The hybrid cathode delivers a higher specific discharge capacity with more defined voltage plateaus and lower polarization than pristine $VSe_2$, confirming improved Zn-ion storage, enhanced charge transfer kinetics and reduced internal resistance[39]. During discharge process, $VSe_2$-MWCNT nanohybrid cathode exhibits well defined plateaus at 0.9 V and 0.55 V corresponding to Zn-ion intercalation into $VSe_2$ structure by reduction of $V^{4+}$ ions to form Zinc intercalated compound: $Zn_xVSe_2$. Upon consecutive charge, the plateaus at 0.71 V and 1.1 V corresponds to the oxidation step of the $Zn_xVSe_2$ to form $VSe_2$ during Zn-ion deintercalation process. The enhanced redox kinetics decreased polarization, and enhanced capacity is also reflected as reduced potential difference between the charging and discharging plateaus ($\Delta E \sim 0.44$ V). The highly reversible nature of Zn-ion storage in $VSe_2$-MWCNT nanohybrid can be further validated with consecutive CV curves. The shape profile of CV curves remained similar, and the highly overlapping CV curves with negligible polarization even 5 cycles (**Figure 3c**) indicate excellent electrochemical reversibility, with strong stability during repeated Zn-ion intercalation/deintercalation processes. The cathodic peaks observed in the CV curves at 0.66 V and 1.1 V are attributed to the following reactions [16]

View Article Online
DOI: 10.1039/D5YA00130G



$VSe_2$-MWCNT + $mZn^{2+}$ + $2me^-$ ⟷ $Zn_mVSe_2$-MWCNT

$Zn_mVSe_2$-MWCNT + $nZn^{2+}$ + $2ne^-$ ⟷ $Zn_{(m+n)}$ $VSe_2$-MWCNT

The shape profiles of CV curves and the redox peak position remained unchanged even after the scan rate was increased to 0.5 mV $s^{-1}$ from 0.1 mV $s^{-1}$ (**Figure 3d**), indicating superior electrochemical resilience in $VSe_2$-MWCNT nanohybrid. The highly reversible nature of the $VSe_2$-MWCNT nano hybrid is shown by nearly intact charge-discharge curves at 0.2 A $g^{-1}$, as shown in **Figure 3e**, which signifies the highly reversible nature of Zn-ion storage in the cathode. Meanwhile, GCD curves shows two discharge plateaus can be clearly distinguished, corresponding to two pairs of redox peaks in CV curves, implying the existence of a two-step Zn-ion insertion/removal process. However, the GCD curves of pristine $VSe_2$ (Figure S3a) shows lower capacity and quick capacity decay upon consecutive cycles than $VSe_2$-MWCNT nano hybrid. The polarization of the charge-discharge curves is also higher than $VSe_2$-MWCNT nano hybrid. The favourable structure of $VSe_2$ and MWCNT composite exhibits improved discharge capacity, coulombic efficiency, and polarization, indicating prompt and reversible Zn-ion storage in the $VSe_2$ cathode.

The rate capability of the composite cathode materials is examined for to ensure application in high power applications. The $VSe_2$-MWCNT nano hybrid has shown excellent rate cyclability (**Figure 3f-g**) with a maximum specific capacity of 208 mAh $g^{-1}$ at 0.2 A $g^{-1}$ and retains a capacity of ~208, 205, 198, 185, 168, 134 mAh $g^{-1}$ at 0.2, 0.4,1, 2, 4, 8 A $g^{-1}$ respectively. Further, when the current rate was reduced to 0.2 A $g^{-1}$, the $VSe_2$-MWCNT demonstrated a remarkable capacity recovery, delivering over ~ 213 mAh $g^{-1}$ capacity. This observation infers structural integrity of the $VSe_2$-MWCNT composite cathode under dynamic electrochemical condition [40]. In contrast the pristine $VSe_2$ cathode provides specific capacity of 150 mAh $g^{-1}$ at 0.2 A $g^{-1}$, which decays to 20 mAh $g^{-1}$at higher current rate of 2 A $g^{-1}$, as shown in **Figure S3b**. The lower capacity, higher polarization and poor capacity recovery at lower current density in pristine is mainly due to poor electronic conductivity of cathode without carbon network. As researchers worldwide have been searching for a suitable cathode material with high capacity and structural stability in dynamic electrochemical conditions, the current work on $VSe_2$-MWCNT shows a promising result in comparison to recently explored cathodes such as α, β, γ-$MnO_2$, $V_2O_5$, $NaV_3O_8$ PANI-CFs TMD cathodes like $VS_2$ and $VS_2$-rGO etc [41,42]. Along with the conductivity and defect sites provided by narrow 2D structure, the well-dispersed and lamellar $VSe_2$ structure is responsible for superior-rate performance of the composite cathode.

View Article Online
DOI: 10.1039/D5YA00130G



The rational design of the $VSe_2$-MWCNT cathode ensures decreased polarization and rapid charge transfer between the 2D stacked $VSe_2$ layers and MWCNT for exceptional rate performance. Moreover, the few layered $VSe_2$ and MWCNTs composite is able to withstand mechanical stress or strain during rapid Zn ion exchange with high-current rate conditions.

The long cyclability of $VSe_2$ cathode was tested at a lower current rate (1 A $g^{-1}$) and also at higher current rate (2 A $g^{-1}$), and the results are given in **Figure 4**. $VSe_2$-MWCNT nanohybrids displays incredible stability along with excellent coulombic efficiency even after 600 cycles when tested at 1 A $g^{-1}$. This suggests the synergistic effect of MWCNT with $VSe_2$ in terms of structural integrity in repeated Zn-ion insertion and extraction process as well as enhanced electrochemical activity [43,44]. When tested at at 2 A $g^{-1}$ **(Figure 4b)**, $VSe_2$-MWCNT nano hybrid cathode showed a stable capacity (600 cycles) after the initial capacity stabilization process. The initial structural stabilization in $VSe_2$ cathode due to the higher charge density and larger size of $Zn^{2+}$ ions contributes could increase the initial capacity slowly and this needs further investigation [45–47]. The $VSe_2$-MWCNT initially shows increasing capacity and after cycles, the capacity becomes almost constant at 185 mAh $g^{-1}$ after 50 cycles. The columbic efficiency of the composite cathode also remained the same indicating highly reversible Zn ion storage. This is attributed to the defects introduced by MWCNT which can also serve as additional sites for Zn absorption [48]. At the higher current density of 2 A $g^{-1}$, a slightly decline in capacity after 300 cycles is observed, when compared to cyclic stability at 1 A $g^{-1}$. Higher current rates will lead to more severe surface reactions due to unwanted electrolyte decomposition, forming resistance layers. The new layers could block the ion access and increasing the internal resistance, resulting in quick capacity fade. Increased overpotential, and polarization due to higher internal resistance will trigger quick capacity fading at higher current. During long-term cycling, a high mechanical stress during zinc ion insertion and extraction at high current rate, leading to cracking and degradation of the electrodes [49]. **Table S1** compares the performance of $VSe_2$-MWCNT cathode over several recently reported vanadium- and transition metal-based cathodes for ZIBs It is clearly seen $VSe_2$-MWCNT cathode outperforms most of recently studied vanadium- and transition metal-based cathodes. $VSe_2$-MWCNT showed higher capacity, superior rate performance, and long stability than other cathodes. The $VSe_2$-MWCNT exhibits superior performance mainly due to synergistic effect of 2D structured $VSe_2$ grown over 1D structured MWCNTs.

The Nyquist impedance plots for $VSe_2$ and $VSe_2$-MWCNT cathodes, shown in **Figure S**4, over a frequency range of 10 mHz - 100 kHz. In the high-frequency range, a semicircle is observed,

View Article Online
DOI: 10.1039/D5YA00130G



indicating the charge transfer resistance ($R_{ct}$). In the low-frequency range, an inclined line represents the Warburg impedance ($W_0$). The resistance originating from the electrolyte and cathode material interface along the line from the origin to the semicircle's cutting point along the real axis is the ohmic resistance ($R_0$). The diameter of the semi-circle decreases, and thereby the charge transfer resistance ($R_{ct}$) decreases, and the length of the inclined line increases with the addition of MWCNT. This implies rapid diffusion of Zn-ion through the cathode material in $VSe_2$-MWCNT nano hybrid than $VSe_2$. The $VSe_2$-MWCNT exhibits an ohmic resistance ($R_0$) of approximately 1.4 ohm and a charge transfer resistance of around 43 ohms. In contrast, pristine $VSe_2$ display an ohmic resistance ($R_0$) 18 Ω and charge transfer resistance ($R_{ct}$) of about 182. The evident of the low $R_{ct}$ and the $R_0$ are attributed to the synergy of $VSe_2$ 2D sheets and the MWCNT conductive network that boosts the storage kinetics [50].

The gravimetric intermittent titration technique (GITT) was utilized to quantitatively examine the Zn-ion diffusion kinetics in with transient voltage change in $VSe_2$-MWCNT nanohybrid cathode. This technique involves quick charging/discharging pulse for 10 min followed by a longer relaxation time of 2 h to attain equilibrium, and this process repeated until full charge/discharge window. The Zn-ion diffusion coefficient during the intercalation/deintercalation process can be calculated from Fick's second law: $\mathbf{D_{Zn} = 4/\pi\tau(m_B V_M/M_W A)_2(\Delta E_S/\Delta E_\tau),}$ where $m_B$, $V_M$, and $M_w$ are the mass, molar volume, and molecular weight of the $VSe_2$ cathode respectively, $\tau$ is time for the applied galvanostatic current (s), $A$ is the specific area of the cathode ($cm^2$), and $\Delta E_s$ and $\Delta E_\tau$ are the pseudo-equilibrium voltage and voltage change during the current pulse (V), respectively. **Figure 5a-b** displays the equilibrium voltage in different Zn-ion intercalation/intercalation steps and the corresponding Zn-ion diffusion coefficients. During discharge state, the maximum Zn-ion diffusion coefficient derived from Fick's second law was 9.74 X $10^{-12}$ $cm^2$ $s^{-1}$ for $VSe_2$-MWCNT nanohybrid [51]. The presence of porous channel network of MWCNT between the two-dimensional $VSe_2$ sheets facilitates prompt diffusion of $Zn^{2+}$ ions inside the cathode materials which reduces the intrinsic resistance of cathode[39,52]. Interestingly, the $VSe_2$-MWCNT composite cathode exhibited a higher Zn-ion diffusion co-efficient than previously studied metal oxides, metal sulfides, and polyanions based cathodes [53–57].The synergy of metallic $VSe_2$ and carbonaceous MWCNTs offer higher active surface area and electron-ion intercalation and deintercalation, this speeds up interfacial charge transfer and minimises undesirable reactions at the cathode side [30,58–61]. The MWCNT eliminate constraints related to

View Article Online
DOI: 10.1039/D5YA00130G



Zn-ion diffusion and result in exceptional electrochemical performances at greater current and power densities.

The rapid Zn-ion storage kinetics of the $VSe_2$-MWCNT nanohybrid cathode was studied from current – voltage relationship through the CV measurements previously taken at different scan rates ranging from 0.1 mV $s^{-1}$ to 0.5 mV $s^{-1}$. The capacitive and diffusion-related reaction kinetics can be demonstrated by the equation [51,62] : $\mathbf{i = a_1v + b_2v^{1/2}}$. Here, $a_1v$ is the capacitive contribution in ion storage, and $b_2v^{1/2}$ is diffusion-influenced reaction kinetics at a specific scan rate. At the scan rate of 0.5 mV $s^{-1}$, the capacitive and diffusive induced current contributions for $VSe_2$-MWCNT nanohybrid is calculated to ~92.65 % and 7.35 % respectively (**Figure 5c**). **Figure 5d** displays the histogram of the percentage of capacitive and diffusive current contributions at scan rates ranging from 0.1 to 0.5 mV $s^{-1}$. It is notable that the capacitive current contribution is intensified with increasing in the scan rate from 0.1 to 0.5 mV $s^{-1}$, and the capacitive contribution is 88.86%, 90.72%, 91.86%, and 92.65 % at 0.2, .03, 0.4, and 0.5 mV $s^{-1}$ respectively. The log(peak current) vs log (scan rate) analysis (**Figure S5a**) provides b-values for peak-1 and peak-2 at 0.59 V and 1.04 V respectively, indicating a combination of diffusion and surface-controlled processes, with the latter Zn-ion storage peak are dominating. At 0.5 mV $s^{-1}$, the $VSe_2$–MWCNT composite exhibited a capacitive contribution of 92.65% (**Figure 5c**) with excellent linearity ($R_1^2$ = 0.998, $R_2^2$ = 0.994) observed at each analysed voltage. To further support the capacitive behaviour storage, claim in $VSe_2$-MWCNT nanohybrid cathode, we restudied the CV analysis and compared the pseudocapacitive behaviour with pristine $VSe_2$, pristine MWCNTs, physically mixed $VSe_2$-MWCNTs, and hydrothermally made $VSe_2$-MWCNT nanohybrid. The pristine $VSe_2$ showed a capacitive contribution of 28.16% for Zn-ion storage (Fig 2b), much lower than VSe2-MWCNT nanohybrid (92.65%) (**Figure S5b**). The pristine MWCNTs showed EDLC type storage behaviour with 85.60% pseudocapacitive contribution (**Figure S5c**), while the physically mixed $VSe_2$ and MWCNT showed only 73.07% pseudocapacitive contribution (**Figure S5d**). These findings clearly demonstrate the superior capacitive performance of the composite, which can be attributed to the synergistic interaction between $VSe_2$ and MWCNTs. The hybrid architecture containing 2D layered $VSe_2$ over 1D multi-walled CNTs synergistic overcome the intrinsic restacking and conductivity limitations of pristine $VSe_2$ to improve electrochemical kinetics and significantly boost the capacitive behaviour. The unique 2D layered structure of $VSe_2$ will facilitate easy ion diffusion between the layers, and allow rapid electron transfer while the MWCNTs has inherent high electronic conductivity, and high surface area. The

View Article Online
DOI: 10.1039/D5YA00130G



composite in synergy can lead to enhanced ion diffusion, contributing to high pseudocapacitance. The presence of defect site in $VSe_2$ will also increase the active site for Zn-ion storage, promoting the surface controlled redox reactions, and thereby increasing the overall pseudocapacitance. The high mechanical strength of MWCNTs will help to prevent any mechanical degradation, helping to retain the pseudocapitance for long cycles. The structure also favoured fast ion adsorption due to effective interface contact between the electrolyte, helping to achieve high capacity at high current rate. A large buffer space generated with MWCNT-2D $VSe_2$ sheets can minimize any severe volume change during the charge/discharge cycle and offer an efficient pathway for Zn-ion flux in the electrode/electrolyte interface. [51].

The **Figure 6a** shows ex-situ XRD of $VSe_2$-MWCNT nanohybrid during Zinc ion storage at different state of charge, giving good insight on structural changes associated with $VSe_2$ cathode during Zn-ion (de)intercalation. **Figure 6 b-e** shows the magnified ex-situ XRD pattern for the (001), peak for MWCNT, (002), and (011) plane, and the continuous peak shifting followed by peak recovery suggest that $VSe_2$ accommodate and release Zn ions without complete structural collapse [34,63]. Figure 6c shows the XRD peak for zinc hydroxide byproduct, a common by-product formed in vanadium-based cathode during battery cycling along with the peaks corresponding to MWCNT. In an aqueous electrolyte, the local environment around the electrolyte can become more alkaline due to the movement of hydroxide ions ($OH^-$) which will interact with zinc ions can react with the hydroxide ions to form zinc hydroxide ($Zn(OH)_2$) by-product. The XRD patterns shows the reversible $Zn^{2+}$ intercalation storage in $VSe_2$ with associated crystalline structural changes, indicating $VSe_2$ as a potential as a cathode for ZIBs. During charge/ discharge process, the possible electrolyte diffusion and zinc-ion insertion/extraction into MWCNTs will alter the interplanar spacing of MWCNTs, leading to peak shifts. In particular, the peak for MWCNTs also shifts to a lower angle compared to due to residual Zn-ion intercalation during charge/discharge process. The sequential shift and recovery of XRD peaks indicate that the $VSe_2$ can accommodate and release Zn ions without complete structural collapse, favourable for long term stability. The chemical changes associated with vanadium during Zn-ion storage is further studied with ex-situ XPS and the results are given in **Figure 6 f and 6 g**. The Zn 2p peaks are absent in $VSe_2$ cathode before cycling, whereas Zn 2p peaks emerge during the discharge process, indicating Zn-ion intercalation into the $VSe_2$ structure. The Zn-ion gets stored due through V reduction and Se environment change, and the two peaks at ~1023 eV and ~1046 eV corresponds to Zn $2p_{1/2}$ and Zn $2p_{3/2}$ peaks confirm that the Zn-ions are stored as $Zn_xVSe_2$ and no formation of $Zn_0$ is noted.

View Article Online
DOI: 10.1039/D5YA00130G



Upon consecutive charge, a less intense characteristic Zn 2p peaks were still observed, indicating that Zn-ions are not fully recovered during the consecutive charge process. The $Zn^{2+}$ ions could get trapped into the $VSe_2$ layers and in the defects, making them detectable in the XPS spectrum. However, this could reduce the active sites for zinc ion intercalation, thereby decreasing ion accessibility and transport within the cathode material. This could also be attributed to confirmation of zinc species containing stable interfacial layer over the cathode [64]. Such type of behaviour is observed in many vanadium based oxides and selenides.

The deconvoluted V2p spectrum before cycling shows the dominant nature of the $V^{4+}$ state in $VSe_2$ along with small amount of $V^{3+}$ due to defects in layered structure [20]. Upon discharging, the intensity of $V^{4+}$ significantly reduced with increase in $V^{3+}$ region, indicating the Zn-ion storage is through $V^{4+}$ reduction to $V^{3+}$. Upon consecutive charge, the valence state of V returns to initial $V^{4+}$, indicating a good reversibility [20,63]. The full width at half maximum (FWHM) values have been calculated for the cathodes at charged, discharged, and pristine states, as shown in the Table S2. The intercalation of zinc ions into the $VSe_2$ layers makes the vanadium valence state reduces from $V^{4+}$ to $V^{3+}$, creating a more homogeneous chemical environment. This results in sharper V 2p peaks and a decreased FWHM. During charging, the material exhibits mixed valence states along with unwanted surface reactions and chemical disorder, which cause broadening of the V 2p peaks and an increased FWHM [65,66].

The change in $VSe_2$ lattices during Zn-ion storage is evaluated with ex-situ HRTEM and HAADF analysis. The **Figure 7** gives the good understanding on the structural reversibility and distribution of intercalated Zn-ions in the $VSe_2$ layers during charge and discharge process. During the discharge state, uniform distribution of Zn-ion over $VSe_2$ cathode is clearly observed through HAADF mapping and The HAADF mapping shows an even distribution of Zn along with V, Se and C. The calculated interplanar spacing for the (011) plane for Zn-ion intercalated $VSe_2$ calculated from the Gray value d-spacing plot, and it has decreased to ~ 0.27 from 0.3 nm, confirming the Zn-ion intercalation into the layered structure. After consecutive charge, the distribution of Zn-ion in $VSe_2$ cathode has been significantly reduced, indicating removal of Zn-ion. However, a slight Zn-ions are distributed over cathode due to irreversibility and is confirming the previous XPS study. The interplanar spacing of $VSe_2$ cathode has returned to near original value (~0.27 nm to ~0.283 nm) for the (011) plane, confirming a good structural reversibility for Zn-ion storage in $VSe_2$. The combined findings of ex-situ XRD, ex-situ XPS, ex-situ HRTEM and electrochemical analysis confirm the reversible nature of the $VSe_2$ cathode for Zn-in storage. The $VSe_2$-MWCNT cathode shows prolonged electrochemical

View Article Online
DOI: 10.1039/D5YA00130G



stability due to reversible structural changes during the process. Although an initial Zn-ion irreversibility is observed in $VSe_2$ cathode, the stability of $VSe_2$-MWCNT nanohybrid is not compromised, as evident from the ultra-long stability towards Zn-ion storage. The detailed mechanism for charge storage in the two-dimensional $VSe_2$ layers during the charging and discharging processes can be given as:

$$VSe_2\text{-MWCNT} + xZn^{2+} + 2xe^- \longleftrightarrow Zn_xVSe_2\text{-MWCNT}$$

The two-dimensional framework of the $VSe_2$ enables rapid and reversible redox mediated Zn-ion storage with unlocking more active sites for the Zn ion adsorption. The 2D layered architecture of $VSe_2$ along with nano carbon support facilitates ultra-fast pseudocapacitive mediated Zn-ion storage, playing a crucial role in the remarkable charge storage performance of $VSe_2$. A strong metallic characteristic of $VSe_2$-MWCNT nano hybrid arising synergistically from 2D $VSe_2$ and MWCTNs, along and robust 2D layered structure, facilitated $VSe_2$ to achieve high capacity, rate and good stability as cathode for Zn-ion batteries. Interestingly, $VSe_2$ cathode exhibited a facile and rapid Zn-ion storage than several previously studied metal oxides, polyanions, and metal sulphide-based cathodes for Zn-ion batteries.

## 4. Conclusion

In summary, 2D $VSe_2$-MWCNT nanohybrid with favourable layered structure was investigated as an effective cathode material for aqueous Zinc-ion batteries. The transition metal chalcogenide-based cathode with strong metallic characteristics and defects undertook a ultra-fast pseudocapacitive type storage to deliver high discharge capacity, superior rate, and robust stability. The nano hybrid cathode can reversibly storage Zinc-ion after initial structural stabilization to achieve a discharge capacity of 214 mAh $g^{-1}$ at 0.2 A $g^{-1}$ and long cycle retention with 98% retention at 1 A $g^{-1}$ after 600 cycles. Several ex-situ characterisations reveal the reversible structural changes in the crystal structure along with fast Zinc-ion diffusion inside the 2D layered cathode, higher than metal oxides/sulfides, achieving high-rate Zinc-ion batteries, effective design strategy of advanced TMDs cathode materials for aqueous zinc ion batteries, offering outstanding rate and long cycle, which is suitable for large scale energy storage technologies**.** The current study effective design strategy for transition metal selenides-based cathode materials with pseudocapacitance type storage for multivalent aqueous batteries with high capacity, and outstanding rate and stability.

## Data availability

View Article Online
DOI: 10.1039/D5YA00130G

Data will be made available upon request from the authors

**Conflict of Interest**

There is no conflict of interest to declare

**Acknowledgment**

Dr. Ranjith Thangavel acknowledges the support from the CPRI Bangalore under the Ministry of Power, Government of India through NPP scheme (NPP/21-26/GD/4)

View Article Online
DOI: 10.1039/D5YA00130G





## References

1. N. Zhang, X. Chen, M. Yu, Z. Niu, F. Cheng and J. Chen, *Chem. Soc. Rev.*, 2020, **49**, 4203–4219.
2. T. Wang, C. Li, X. Xie, B. Lu, Z. He, S. Liang and J. Zhou, *ACS Nano*, 2020, **14**, 16321–16347.
3. L. Chen, Q. An and L. Mai, *Adv. Mater. Interfaces*, 2019, **6**, 1900387.
4. X. Zhao, X. Liang, Y. Li, Q. Chen and M. Chen, *Energy Storage Mater.*, 2021, **42**, 533–569.
5. N. Mohamed and N. K. Allam, *RSC Adv.*, 2020, **10**, 21662–21685.
6. W. Lee, S. Muhammad, C. Sergey, H. Lee, J. Yoon, Y. M. Kang and W. S. Yoon, *Angew. Chem. Int. Ed.*, 2020, **59**, 2578–2605.
7. M. Devi, B. Moorthy and R. Thangavel, *Sustainable Energy Fuels*, 2023, **7**, 3776–3795.
8. H. Shuai, R. Liu, W. Li, X. Yang, H. Lu, Y. Gao, J. Xu and K. Huang, *Adv. Energy Mater.*, 2023, **13**, 2202992.
9. K. Yang, Y. Hu, T. Zhang, B. Wang, J. Qin, N. Li, Z. Zhao, J. Zhao and D. Chao, *Adv. Energy Mater.*, 2022, **12**, 2202671.
10. X. Ma, X. Cao, M. Yao, L. Shan, X. Shi, G. Fang, A. Pan, B. Lu, J. Zhou and S. Liang, *Adv. Mater.*, 2022, **34**, 2105452.
11. Z. Liu, R. Wang, Q. Ma, J. Wan, S. Zhang, L. Zhang, H. Li, Q. Luo, J. Wu, T. Zhou and J. Mao, *Adv. Funct. Mater.*, 2024, **34**, 2214538.
12. M. Song, H. Tan, D. Chao and H. J. Fan, *Adv. Funct. Mater.*, 2018, **28**, 1802564.
13. B. Wu, G. Zhang, M. Yan, T. Xiong, P. He, L. He, X. Xu and L. Mai, *Small*, 2018, **14**, 1703850.
14. Y. An, Y. Tian, Q. Man, H. Shen, C. Liu, Y. Qian, S. Xiong, J. Feng and Y. Qian, *ACS Nano*, 2022, **16**, 6755–6770.
15. Y. Zhang, F. Wan, S. Huang, S. Wang, Z. Niu and J. Chen, *Nat. Commun.*, 2020, **11**, 2199.
16. T. Zhou, L. Zhu, L. Xie, Q. Han, X. Yang, L. Chen, G. Wang and X. Cao, *J. Colloid Interface Sci.*, 2022, **605**, 828–850.
17. L. Zhu, P. Ge, L. Xie, Y. Miao and X. Cao, *Electrochem. Commun.*, 2020, **115**, 1067.
18. X. Jia, C. Liu, Z. G. Neale, J. Yang and G. Cao, *Chem. Rev.*, 2020, **120**, 7795–7866.
19. W. Liu, J. Hao, C. Xu, J. Mou, L. Dong, F. Jiang, Z. Kang, J. Wu, B. Jiang and F. Kang, *Chem. Commun.*, 2017, **53**, 6872–6874.
20. Y. Bai, H. Zhang, B. Xiang, X. Liang, J. Hao, C. Zhu and L. Yan, *ACS Appl. Mater. Interfaces*, 2021, **13**, 23230–23238.
21. P. He, M. Yan, G. Zhang, R. Sun, L. Chen, Q. An and L. Mai, *Adv. Energy Mater.*, 2017, **7**, 1700464.
22. R. Zhang, C. Pan, R. G. Nuzzo and A. A. Gewirth, *J. Phys. Chem. C*, 2019, **123**, 8740–8745.
23. Y. Tang, X. Li, H. Lv, D. Xie, W. Wang, C. Zhi and H. Li, *Adv. Energy Mater.*, 2020, **10**, 2000892.

View Article Online
DOI: 10.1039/D5YA00130G



24. Y. Jin, M. E. Lee, G. Kim, H. Seong, W. Nam, S. K. Kim, J. H. Moon and J. Choi, *Materials*, 2023, **16**, 1253.
25. M. Yan, X. Pan, P. Wang, F. Chen, L. He, G. Jiang, J. Wang, J. Z. Liu, X. Xu, X. Liao and J. Yang, *Nano Lett.*, 2017, **17**, 4109–4115.
26. A. V. Murugan, C. S. Gopinath and K. Vijayamohanan, *Electrochem. Commun.*, 2005, **7**, 213–218.
27. Q. Li, W. Zhang, J. Peng, D. Yu, Z. Liang, W. Zhang, J. Wu, G. Wang, H. Li and S. Huang, *Adv. Funct. Mater.*, 2022, **32**, 2112776.
28. M. Rani, M. Sehrawat, S. Sharma and B. P. Singh, *J. Energy Storage*, 2023, **73**, 109063.
29. K. K. Gangu, S. Maddila, S. B. Mukkamala and S. B. Jonnalagadda, *J. Energy Chem.*, 2019, **30**, 132–144.
30. P. Siddu, S. R. K. A, S. Radhakrishnan, S. M. Jeong and C. S. Rout, *Batteries & Supercaps*, 2025, **8**, e202400466.
31. A. S. Sree, B. Shajahan, B. Chakraborty and C. S. Rout, *RSC Adv.*, 2020, **10**, 31712–31719.
32. M. Narayanasamy, L. Hu, B. Kirubasankar, Z. Liu, S. Angaiah and C. Yan, *J. Alloys Compd.*, 2021, **882**, 160704.
33. G. D. Park, J. H. Kim, S. K. Park and Y. C. Kang, *ACS Appl. Mater. Interfaces*, 2017, **9**, 10673–10683.
34. L. Wang, Z. Wu, M. Jiang, J. Lu, Q. Huang, Y. Zhang, L. Fu, M. Wu and Y. Wu, *J. Mater. Chem. A*, 2020, **8**, 9313–9321.
35. W. Oh, H. Park, B. S. Jin, R. Thangavel and W. S. Yoon, *J. Mater. Chem. A*, 2020, **8**, 10331–10336.
36. R. Thangavel, D. Han, B. Moorthy, B. K. Ganesan, M. Moorthy, Y. Park, K. W. Nam and Y. S. Lee, *Small Methods*, 2022, **6**, 2100888.
37. Z. Wu, C. Lu, Y. Wang, L. Zhang, L. Jiang, W. Tian, C. Cai, Q. Gu, Z. Sun and L. Hu, *Small*, 2020, **16**, 2000698.
38. T. G. Park, B. K. Choi, J. Park, J. Kim, Y. J. Chang and F. Rotermund, *ACS Nano*, 2021, **15**, 7756–7764.
39. V. Soundharrajan, S. Nithiananth, J. Lee, K. Sakthiabirami, D. T. Pham, J. H. Kim, J. Y. Hwang and J. Kim, *J. Power Sources*, 2023, **558**, 232542.
40. D. Xie, Y. Sang, D. H. Wang, W. Y. Diao, F. Y. Tao, C. Liu, J. W. Wang, H. Z. Sun, J. P. Zhang and X. L. Wu, *Angew. Chem. Int. Ed.*, 2023, **62**, e202216934.
41. L. Chen, Q. An and L. Mai, *Adv. Mater. Interfaces*, 2019, **6**, 1900387.
42. S. Li, P. Das, X. Wang, C. Li, Z. S. Wu and H. M. Cheng, *Small*, 2025, **na**, 2410036.
43. H. Lu, J. Hu, Y. Zhang, K. Zhang, X. Yan, H. Li, J. Li, Y. Li, J. Zhao and B. Xu, *Adv. Mater.*, 2023, **35**, 2209886.
44. W. Cui, J. Wang, Y. Li, P. Liu and F. Dong, *Environ. Sci.: Nano*, 2025, **12**, 67–97.
45. L. Wang, Z. Wu, M. Jiang, J. Lu, Q. Huang, Y. Zhang, L. Fu, M. Wu and Y. Wu, *J. Mater. Chem. A*, 2020, **8**, 9313–9321.
46. X. Chen, X. Hu, Y. Chen, X. Cao, Y. Huang, H. Zhang, J. H. Liu, Y. Wang, S. L. Chou and D. Cao, *J. Mater. Chem. A*, 2022, **10**, 22194–22204.
47. X. Zhu, W. Wang, Z. Cao, S. Gao, M. O. L. Chee, X. Zhang, P. Dong, P. M. Ajayan, M. Ye and J. Shen, *J. Mater. Chem. A*, 2021, **9**, 17994–18005.

View Article Online
DOI: 10.1039/D5YA00130G



48. Q. Liu, K. Yang, Z. Wang, S. Chen, W. Zhang, H. Ma, X. Geng, Q. Deng, Q. Zhao and N. Zhu, *ACS Appl. Mater. Interfaces*, 2024, **16**, 20610–20617.
49. G. Li, L. Sun, S. Zhang, C. Zhang, H. Jin, K. Davey, G. Liang, S. Liu, J. Mao and Z. Guo, *Adv. Funct. Mater.*, 2024, **34**, 2301291.
50. X. Cui, Y. Li, Y. Zhang, Z. Sun, Y. Liu, J. Zhang, E. Xie and J. Fu, *Chem. Eng. J.*, 2023, **478**, 147197.
51. V. Soundharrajan, S. Nithiananth, J. Lee, J. H. Kim, J. Y. Hwang and J. Kim, *J. Mater. Chem. A*, 2022, **10**, 18162–18169.
52. V. Soundharrajan, J. Lee, S. Kim, J. H. Kim, J. Y. Hwang and J. Kim, *Batteries & Supercaps*, 2023, **6**, e202200527.
53. J. Jiang, H. Li, J. Huang, K. Li, J. Zeng, Y. Yang, J. Li, Y. Wang, J. Wang and J. Zhao, *ACS Appl. Mater. Interfaces*, 2017, **9**, 28486–28494.
54. Y. Gao, H. Yang, X. Wang, Y. Bai, N. Zhu, S. Guo, L. Suo, H. Li, H. Xu and C. Wu, *ChemSusChem*, 2020, **13**, 732–740.
55. L. Geng, J. P. Scheifers, C. Fu, J. Zhang, B. P. T. Fokwa and J. Guo, *ACS Appl. Mater. Interfaces*, 2017, **9**, 21251–21257.
56. Q. Pang, S. Yang, X. Yu, W. He, S. Zhang, Y. Tian, M. Xing, Y. Fu and X. Luo, *J. Alloys Compd.*, 2021, **885**, 161008.
57. X. Yang, Q. Sun, L. Chai, S. Chen, W. Zhang, H. Y. Yang and Z. Li, *Small*, 2024, **20**, 2400335.
58. Y. Bai, H. Zhang, H. Song, C. Zhu, L. Yan, Q. Hu and C. M. Li, *Nano Energy*, 2024, **120**, 109090.
59. J. H. Jo, Y. Aniskevich, J. Kim, J. U. Choi, H. J. Kim, Y. H. Jung, D. Ahn, T.-Y. Jeon, K. S. Lee, S. H. Song, H. Kim, G. Ragoisha, A. Mazanik, E. Streltsov and S. T. Myung, *Adv. Energy Mater.*, 2020, **10**, 2001595.
60. F. Wan, L. Zhang, X. Dai, X. Wang, Z. Niu and J. Chen, *Nat. Commun.*, 2018, **9**, 1656.
61. M. H. Alfaruqi, V. Mathew, J. Song, S. Kim, S. Islam, D. T. Pham, J. Jo, S. Kim, J. P. Baboo, Z. Xiu, K.-S. Lee, Y.-K. Sun and J. Kim, *Chem. Mater.*, 2017, **29**, 1684–1694.
62. R. Thangavel, A. Samuthira Pandian, H. V. Ramasamy and Y. S. Lee, *ACS Appl. Mater. Interfaces*, 2017, **9**, 40187–40196.
63. Y. Yi, X. Du, Z. Zhao, Y. Liu, H. Guan, X. Liu, X. Pei, S. Zhang and D. Li, *ACS Nano*, 2022, **16**, 7772–7782.
64. W. Kukułka, V. Montes-García, S. Sarwar, D. Pakulski, P. Samorì and A. Ciesielski, *J. Mater. Chem. A*, 2025, **Doi: 10.1039/D5TA03330F**.
65. Y. Li, C. Zhao, A. Abdukader and X. Wu, *RSC Adv.*, 2024, **14**, 9594–9601.
66. J. Światowska-Mrowiecka, V. Maurice, S. Zanna, L. Klein and P. Marcus, *Electrochim. Acta*, 2007, **52**, 5644–5653.

View Article Online
DOI: 10.1039/D5YA00130G



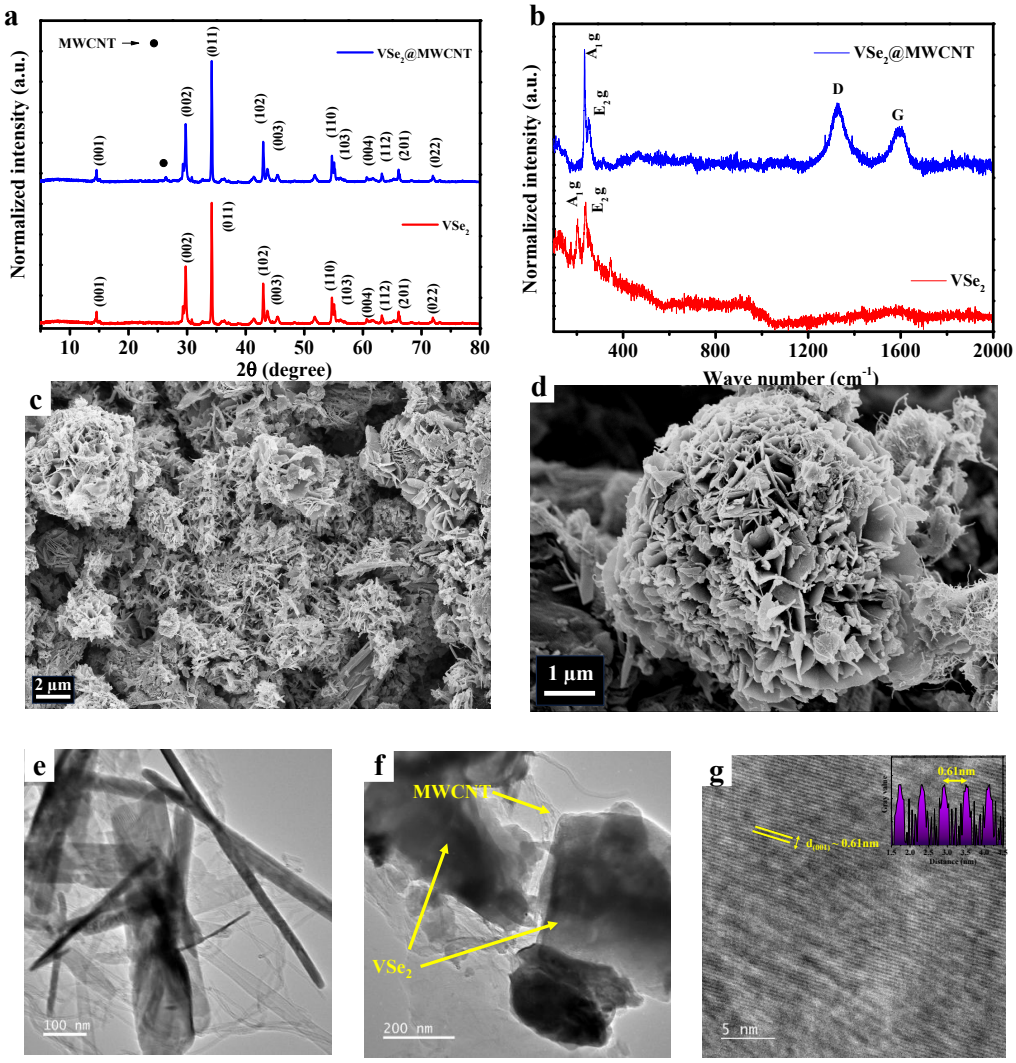


**Fig. 1** (a) XRD plots of $VSe_2$ and $VSe_2$-MWCNT hybrids, (b) Raman spectrum of $VSe_2$ and $VSe_2$-MWCNT hybrids, (c)-(d) FESEM images of $VSe_2$-MWCNT hybrids, (e)-(f) TEM images of and $VSe_2$-MWCNT hybrids, and (g) HR-TEM image of of $VSe_2$-MWCNT.

View Article Online
DOI: 10.1039/D5YA00130G



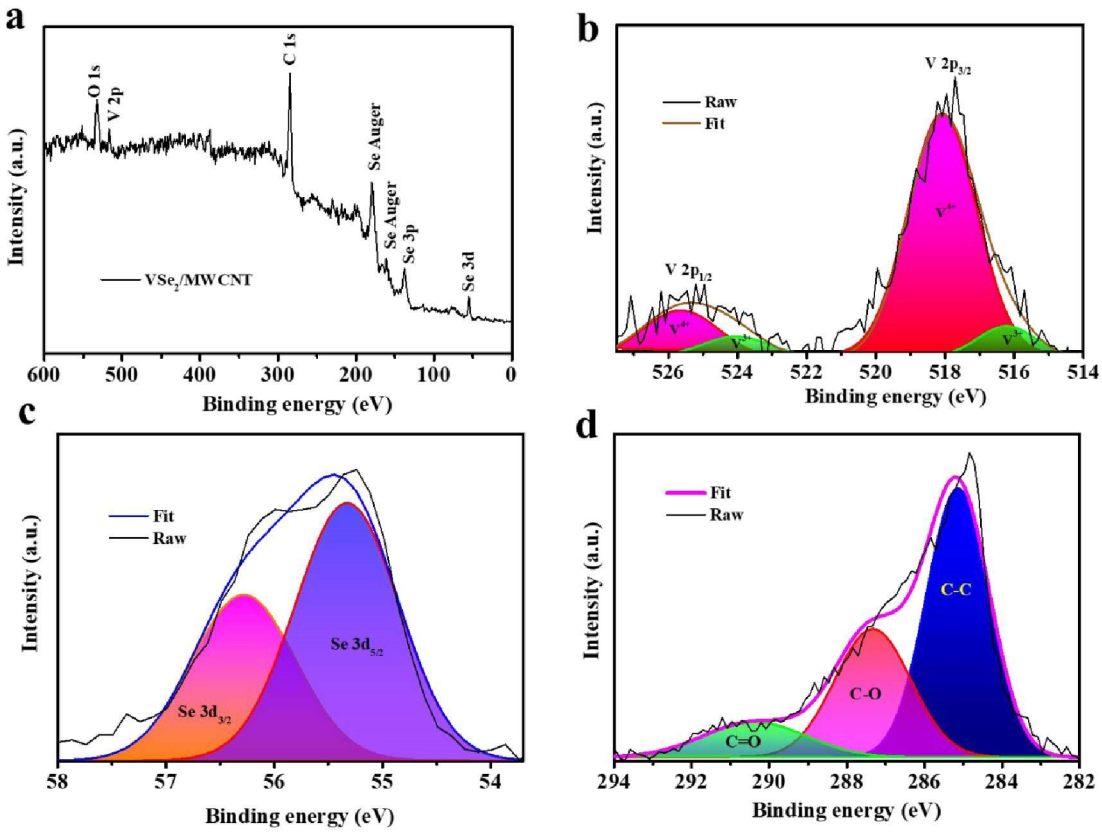


**Fig. 2** (a), Full scale XPS survey for $VSe_2$-MWCNT (b) magnified and deconvoluted XPS spectrum: (b) V 2p peak, (c) Se 3d, and (d) C 1s peak.

View Article Online
DOI: 10.1039/D5YA00130G



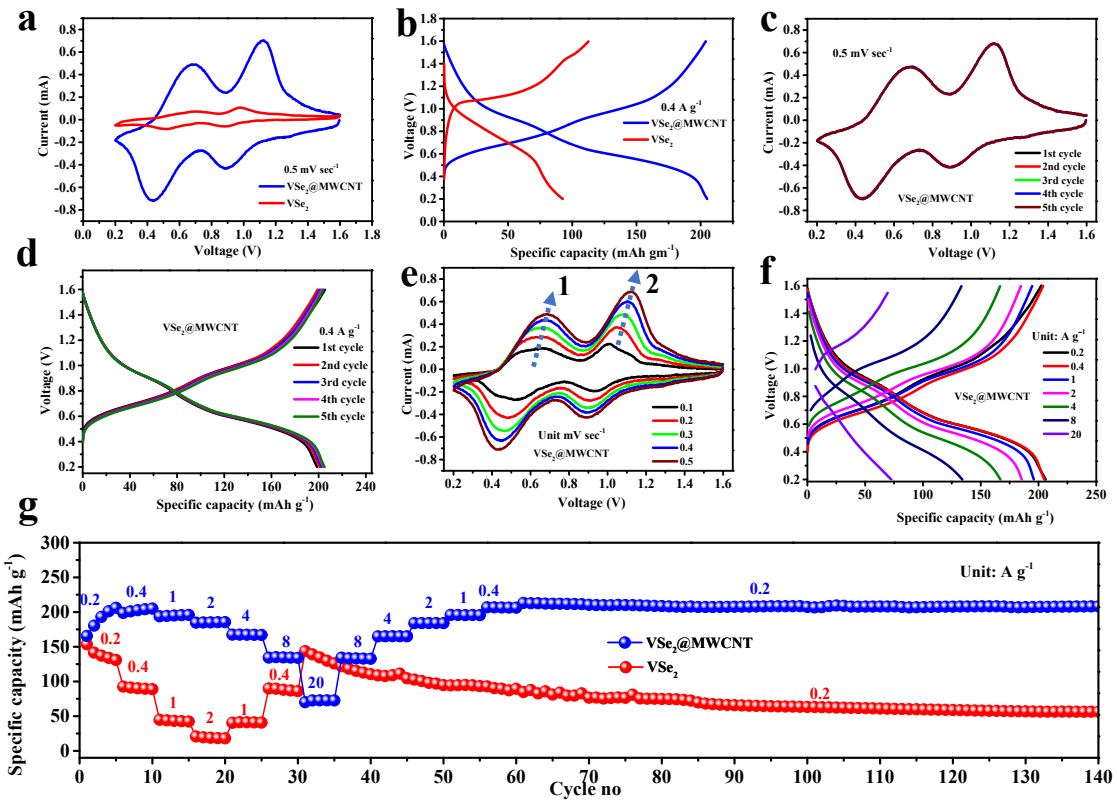


**Fig. 3** Electrochemical performance : (a) cyclic voltammetry (CV) curves at 0.5 mV $s^{-1}$, (b) galvanostatic charge–discharge (GCD) plot, (c) CV curves of $VSe_2$-MWCNT at different cycles (0.5 mV $s^{-1}$), (d) CV curves of $VSe_2$-MWCNT at different scan rates, (e) GCD curves at 0.4 A $g^{-1}$, (f) GCD curves at different current densities, and (g) rate performance of $VSe_2$-MWCNT and pristine $VSe_2$ cathodes.

View Article Online
DOI: 10.1039/D5YA00130G



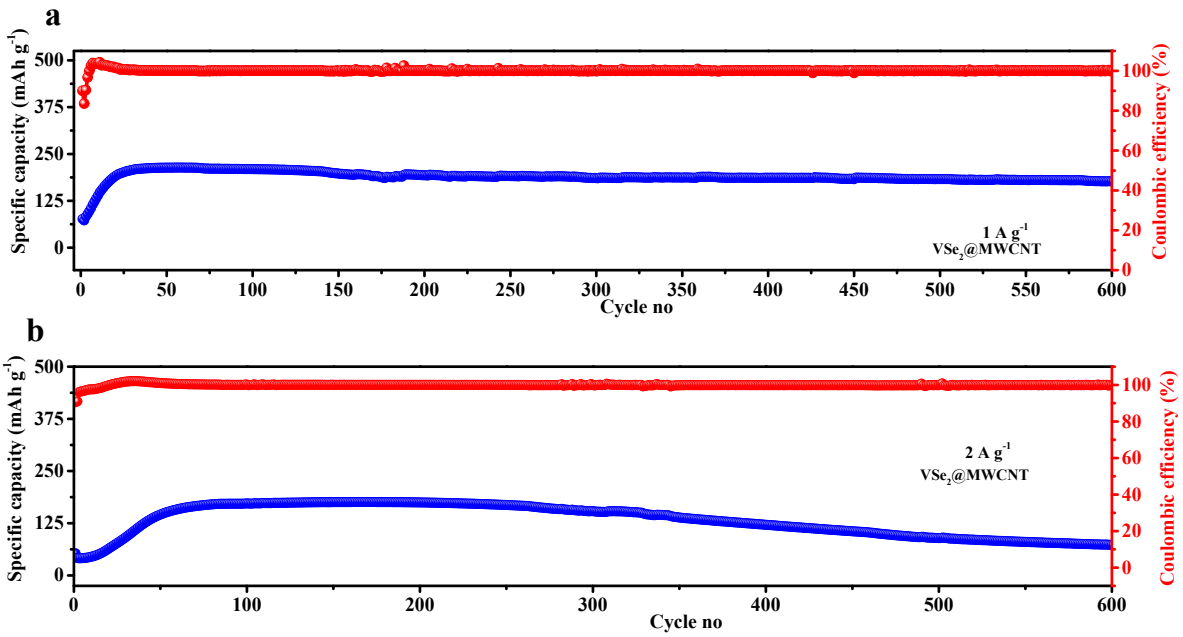


**Fig. 4** Long term cyclic stability of $VSe_2$-MWCNT cathode: (a) at 1 A $g^{-1}$, and (b) 2 A $g^{-1}$.

View Article Online
DOI: 10.1039/D5YA00130G



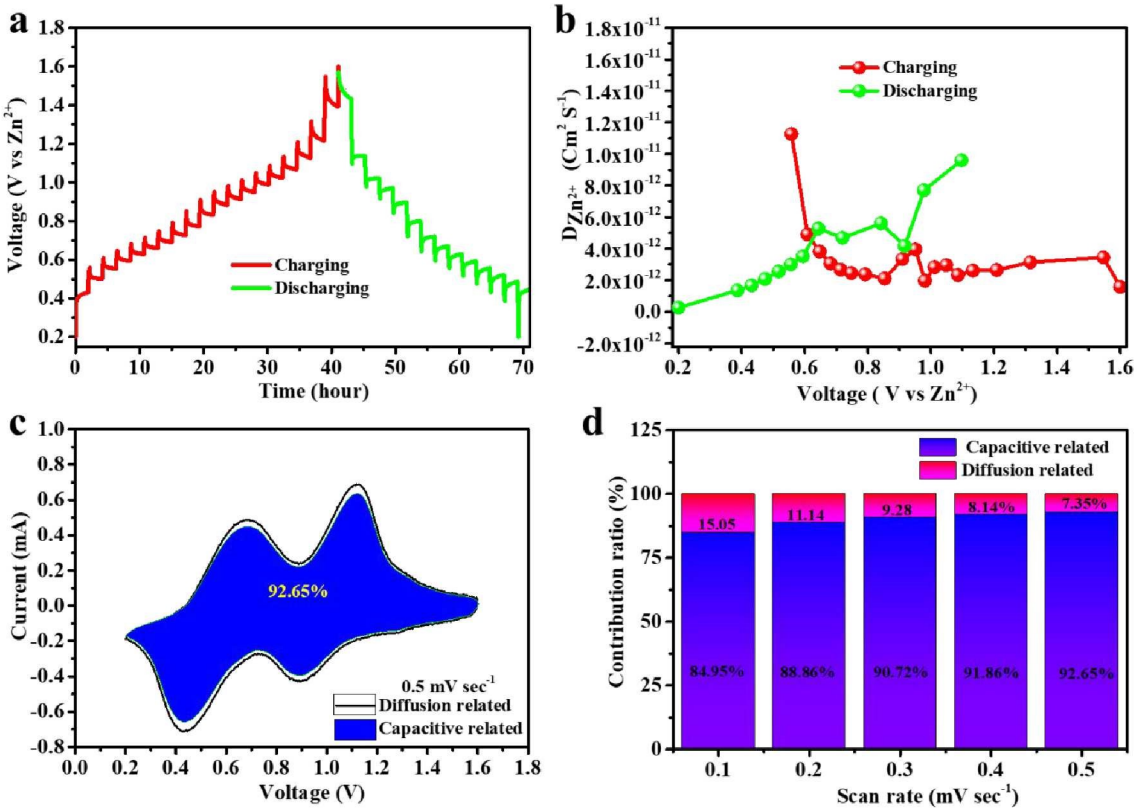


**Fig. 5** (a) GITT: voltage VS time plot of $VSe_2$-MWCNT nanohybrid, (b) diffusivity vs voltage plot of $VSe_2$-MWCNT (c) capacitive contribution of $VSe_2$-MWCNT at scan rate of 0.5 mV $s^{-1}$ and (d) capacitive and diffusive contribution at different scan rate for $VSe_2$-MWCNT.

View Article Online
DOI: 10.1039/D5YA00130G



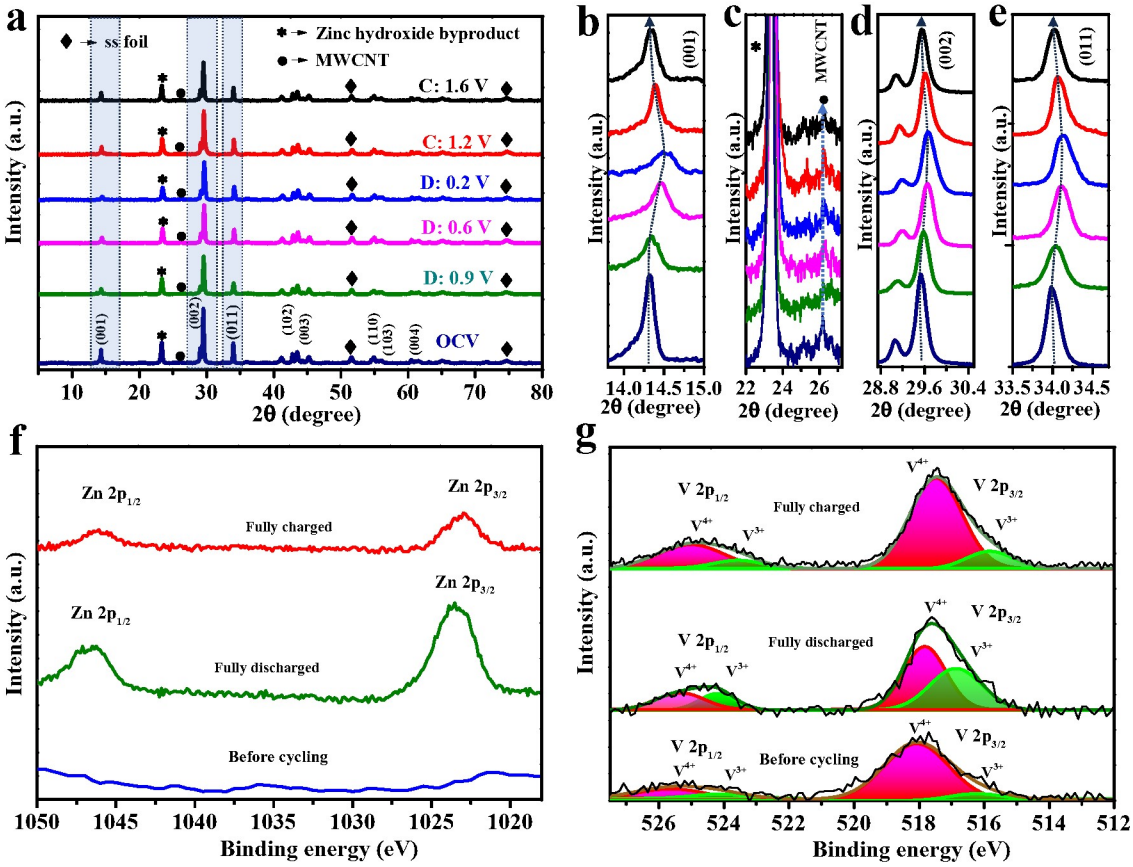


**Fig. 6** (a) Ex situ XRD plots of $VSe_2$–MWCNT at different charge states, (b)–(e) magnified ex situ XRD plots corresponding to the (001) plane, MWCNT and zinc hydroxide byproduct, (002) plane, and (011) plane, respectively, (f) comparison of XPS spectra of $VSe_2$–MWCNT in the charged and discharged states, and (g) deconvoluted V 2p XPS spectra in the charged and discharged states.

View Article Online
DOI: 10.1039/D5YA00130G



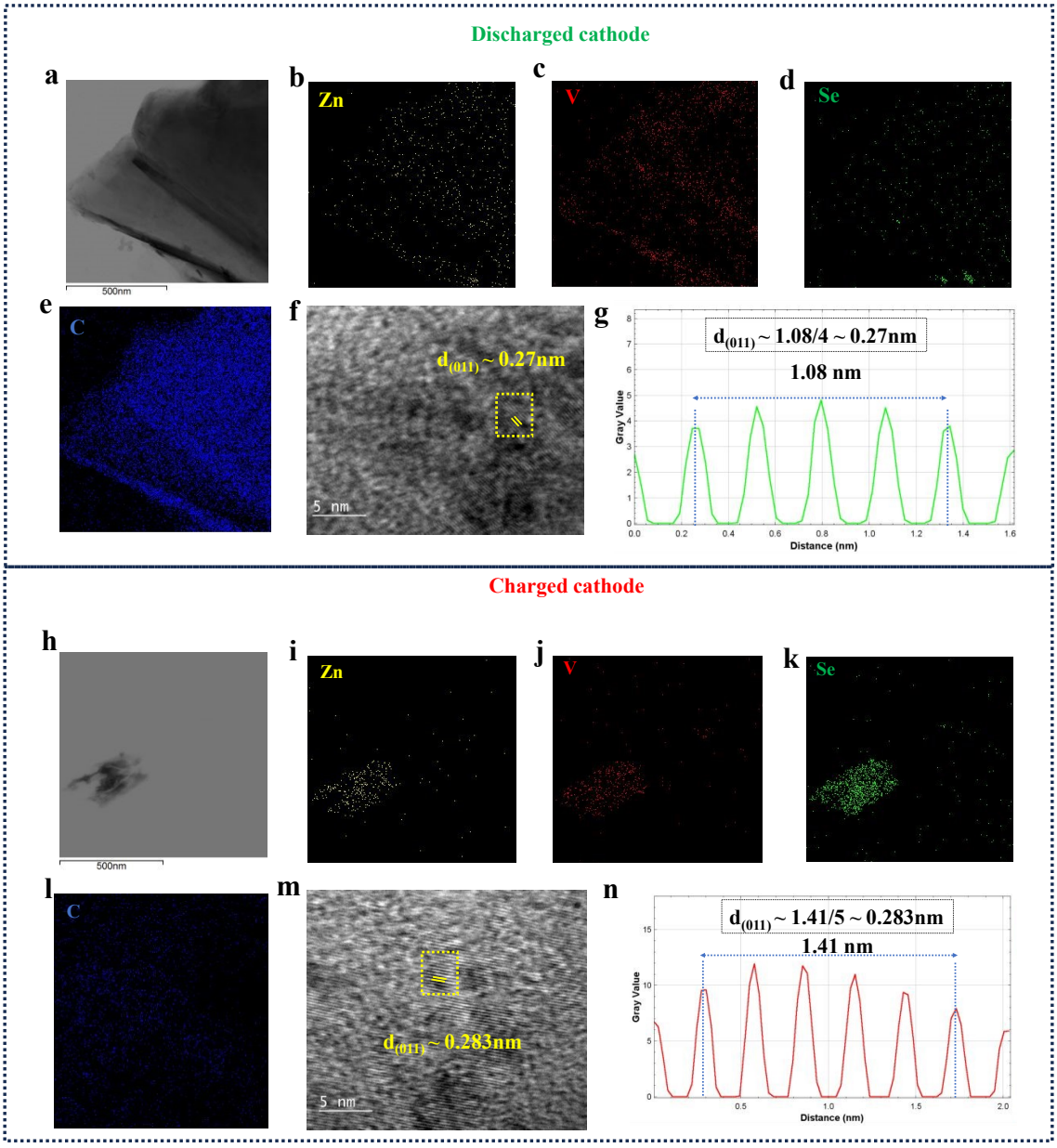


**Fig. 7** FE-TEM, HR-TEM images, HADDF mapping, and corresponding Gray value vs distance plot of $VSe_2$-MWCNT at (a) discharged state, and (b) charged state, yellow box indicates the scanned region for Gray value VS distance plots.

View Article Online
DOI: 10.1039/D5YA00130G

## Data availability

The data are available from the corresponding author on reasonable request.